Evaluating the failure load of high-rise reinforced concrete walls under fire loading using the yield design approach

Mingguan Yang, Duc Toan Pham, Jérémy Bleyer, Patrick de Buhan

Version of Record: https://www.sciencedirect.com/science/article/pii/S2352012422012589
Manuscript_e7eeb6d06f95c44e585a2f3f2c3edac1

Evaluating the failure load of high-rise reinforced concrete walls under fire loading using the yield design approach

Authors: Mingguan Yang[1,2], Duc Toan Pham[1,*], Jérémy Bleyer[2] and Patrick de Buhan[2]

[1] Centre Scientifique et Technique du Bâtiment (CSTB), 84 avenue Jean Jaurès, Champs-sur-Marne, 77447 Marne-la-Vallée Cedex 2, France

[2] Laboratoire Navier (Ecole des Ponts ParisTech, Université Gustave Eiffel, CNRS UMR 8205), 6-8 avenue Blaise Pascal, Cité Descartes, Champs-sur-Marne, 77455 Marne-la-Vallée Cedex 2, France

* Corresponding author: Duc Toan Pham

Email: ductoan.pham@cstb.fr

ABSTRACT : The present contribution is addressing the investigation on the failure of high-rise reinforced concrete walls subject to fire loading. In Yang (2018), a 2D plate model has been developed for predicting the deflections and subsequent geometry changes of tall reinforced concrete panels under severe fire exposure. Such a deformed geometry of the wall is a key ingredient to its stability analysis by means of the yield design theory, which is the subject of the present paper. The practical implementation of the approach is based on shell finite elements and a generalized strength criterion accounting for reduced strength capacities of the constitutive materials. For illustrative purpose, numerical simulations based on typical values of input data (geometrical as well as material parameters), are conducted to investigate the sensitivity of the wall stability to the temperature increase on the one hand, and to its geometrical parameters and boundary conditions, on the other hand. One of the main conclusions which can be drawn from the present analysis is that the boundary conditions prescribed along the vertical lateral sides of the wall have a decisive influence on its stability.

Keywords: *high-rise wall*; *reinforced concrete*; *fire loading*; *yield design*; *stability factor*.

1. INTRODUCTION

Evaluating the ultimate load bearing capacity of reinforced concrete structural members subjected to fire exposure in order to devise appropriate safety design methods, has attracted a growing attention in the last decades, giving rise to an ever-increasing number of theoretical as well as experimental contributions to this crucial issue. One may quote, among many others, the investigations performed by Lie and Celikkol, 1991; Lie and Irwin, 1993; Dotreppe *et al.* 1999; Franssen and Dotreppe, 2003 or El Fatni and Youssef, 2009, who more specifically focused their attention on the fire resistance of reinforced concrete columns exposed to fire.

A convenient way for assessing the strength of reinforced concrete columns consists in deriving the classical axial force-bending moment (*N*-*M*) interaction diagrams and its evolution as a function of the fire-induced temperature gradient (Caldas *et al.* 2010; Law and Gillie, 2010). To this end, the yield design theory with its lower and upper bounds methods (Chen, 1982; Salençon, 2013) provides the most appropriate framework for determining such interaction diagrams in a rigorous way, either under ambient temperature (Averbuch, 1996; Koechlin and Potapov, 2007) or under the action of a temperature gradient (Pham *et al.* 2015a).

As regards the analysis and design of load bearing reinforced concrete walls or panels, the thermomechanical behaviour and more specifically the fire resistance of such structural elements has been investigated by developing appropriate material constitutive models (including plasticity, damage or micro-cracking), associated with the use of numerical (mainly fem-based) methods. One may quote some relevant contributions to the subject such as Talamona and Franssen, 2005; Gernay and Franssen, 2015; Kumar and Kodur, 2017; Roy and Matsagar, 2020 or Jianga *et al.* 2015, who analysed the performance of a very high tower against fire-induced progressive collapse with a help of a dedicated computer software.

Quite frequently involved in the construction of tall industrial buildings, high-rise concrete walls are large size (height) reinforced concrete structures for which the evaluation of the fire resistance requires a more sophisticated approach than for smaller size structures. Indeed, the sole local degradation of the stiffness and strength properties of the reinforced concrete constituent materials (plain concrete and steel reinforcements) due to a severe temperature increase, cannot alone explain the collapse of these structures. Due to the thermal expansion of the reinforced concrete materials, such slender structures may experience important out-of-plane (horizontal) displacements, leading to an eccentricity of the vertical load (self-weight w) with respect to the initial vertical position of the structure. As a consequence, bending moments are generated along the wall in addition to the pre-existing compressive axial force distribution, which is usually known as a second order (or P-δ) effect (Bazant and Cedolin, 2010).

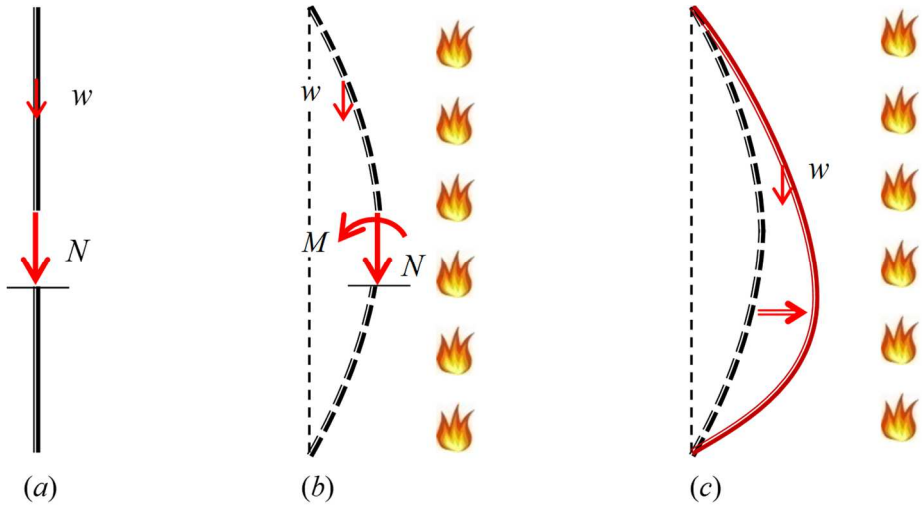

Fig. 1. Schematic side views of a wall (*a*) in its initial vertical configuration; (*b*) subject to pure thermal deformations; (*c*) in its final equilibrium configuration

As the out-of-plane displacements develop, the moments due to self-weight eccentricity increase accordingly, leading to higher bending moments and associated bending curvature deformations, and so on until a final equilibrium configuration is reached (see Fig. 1). At the same time, but independently, elevated temperature leads to degradation of the constituent material properties, and notably their strength properties. It is therefore the conjunction of the

temperature-induced material strength degradation and of the developing bending effects in the wall due to its change of geometry that may trigger the overall failure of the structure, even well before the occurrence of any buckling phenomenon.

Based upon the above general considerations, a three-step analysis procedure may be set up as sketched in Fig. 2.

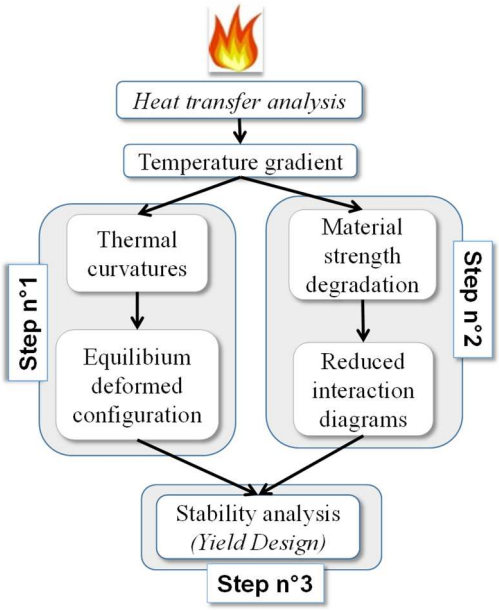

Fig. 2. General three-step analysis procedure for the yield design of fire loaded high rise walls

This procedure has been successfully implemented in the particular case when the wall can be modelled as a *one-dimensional (1D) curved beam* (see Fig. 1). A detailed presentation of this procedure and its applications may be found in Pham, 2014 and Pham *et al.* 2015a; 2015b. The whole procedure is greatly simplified by the adoption of this 1D model, since in such a case, the wall appears to be a *statically determinate* structure, allowing to calculate both axial force and bending moment distributions along the deformed wall from equilibrium considerations only. Unfortunately, the actual configuration of a high-rise walls is more realistically modelled as a *two-dimensional (2D) plate*, than as 1D beams. The objective of this contribution is therefore to extend the above-described procedure to such a plate model.

The implementation of *step n°1* of the general procedure, aimed at calculating the final equilibrium deformed shape of the wall under fire loading, may be found in Yang, 2018. This allows for determining the thermo-elastically deformed geometry of walls subject to the combined action of thermal loading (prescribed temperature gradient across the wall thickness) and gravity forces (self-weight). While the use of a linearized *Love-Kirchhoff* plate model proved to be sufficient for moderately high structures (say less than 8 m), it has been shown that employing the more sophisticated non-linear *von Karman* plate model was required for taking the "*P-δ effect*" into account and predicting the deformed configuration of taller structures which may be involved in the construction of large size-industrial buildings (see Yang, 2018 for more details).

As shown by the general *three-step* design procedure (see Fig. 2), the implementation of *step n°1* is indispensable to the implementation of the yield design calculation (*step n°3*), along with the preliminary determination of the wall strength capacities performed in *step n°2*. The objective of the present paper is to develop these two latter steps which are both based upon the yield design theory, either at the *local* (*step n°2*) or *global* (*step n°3*) level.

Step n°2, which is completely independent of *step n°1*, is devoted to the determination of the strength capacities at any point of the wall, modelled as a plate, expressed by means of a failure condition involving membranes forces and bending moments, *i.e.* the equivalent of interaction diagrams for 1D beams (Pham *et al.* 2015a). The "upscaling" procedure which will be used for deriving such a failure condition, is very similar to that employed for the determination of the thermo-elastic behaviour of a heated plate (Yang (2018)). It is based on the solution to an auxiliary yield design problem defined on a three-dimensional representative reinforced concrete plate element, where the reduced strength capacities of both the concrete material and steel reinforcement, due to elevated temperature, are taken into account.

Step n°3 deals with the yield design-based analysis of the whole structure, relying on two kinds of input data: the deformed geometry of the wall calculated from *step n°1* on the one hand, the reduced strength capacities at any point of the wall obtained as a result of *step n°2* on the other hand.

2. *STEP N°2*: REDUCED STRENGTH DOMAIN OF REINFORCED CONCRETE PLATE SUBJECT TO A TEMPERATURE GRADIENT

The objective of this section, entirely devoted to the implementation of *step n°2* in the case when the wall is modelled as a two-dimensional plate, is to determine the strength properties of a representative reinforced concrete plate element expressed in terms of generalized stresses, namely membrane forces $\underline{\underline{N}}$ and bending moments $\underline{\underline{M}}$. It is more specifically focused on examining the influence of the fire-induced temperature gradient on the degradation of these strength capacities in much the same way as it has been previously achieved for a beam element (Pham *et al.* 2015a). The analysis starts from the required knowledge of the *local* strength degradation of the reinforced concrete individual components: plain concrete and steel reinforcing bars.

2.1. Temperature-induced local strength reduction of plain concrete and reinforcing bars

The effect of temperature on the *local* material strength properties is taken into account by means of three non-dimensional *reduction factors* denoted by $k_c(T)$, $k_t(T)$ and $k_s(T)$ depending on the local temperature $T(\underline{\xi})$. Assuming that the thermal action is homogenous on the fire-exposed wall face, the temperature distribution in the plate thickness is a function of coordinate ξ_3 only, so that the reduced strength properties of the plain concrete and reinforcement steel may be expressed as:

$$f_c(\xi_3) = k_c\left(T(\xi_3)\right) f_c,\ \ f_t(\xi_3) = k_t\left(T(\xi_3)\right) f_t,\ \ \ f_y(\xi_3) = k_s\left(T(\xi_3)\right) f_y \tag{1}$$

where f_c (resp. f_t) denotes the uniaxial compressive (resp. tensile) resistance of plain concrete while f_y is uniaxial yield strength of reinforcing steel at *ambient* temperature. The reduction factors, which are by definition equal to 1 at ambient temperature, are decreasing functions of temperature as specified by Eurocode 2 Part 1-2 (EN 1992-1-2, 2004) and shown in Fig. 3.

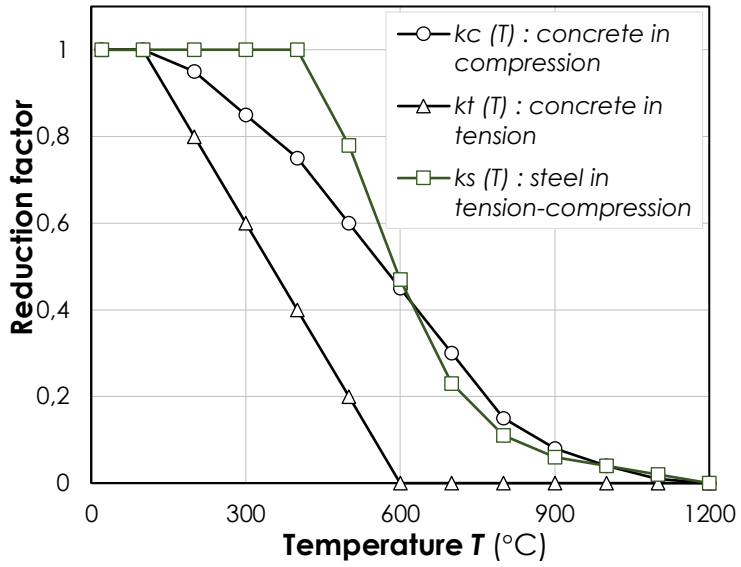

Fig. 3. Example of reduction factors as decreasing functions of temperature (EN 1992-1-2, 2004)

The strength criterion adopted for the plain concrete material, regarded as a three-dimensional continuum, is a *tension cut-off Mohr-Coulomb* condition (Chen, 1982; Marti, 1985; Nielsen and Hoang, 2010) defined as:

$$\underline{\underline{\sigma}} \in G_c(\xi_3) \Leftrightarrow F_c(\underline{\underline{\sigma}}) = \sup\left\{K_p\sigma_M - \sigma_m - f_c(\xi_3)\ ;\ \sigma_M - f_t(\xi_3)\right\} \le 0 \qquad (2)$$

where $\underline{\underline{\sigma}}$ is the stress tensor, σ_M and σ_m its major and minor principal components and $K_p = (1+\sin\varphi)/(1-\sin\varphi)$, where φ is the *internal friction angle* which is usually taken equal to $\varphi = 37°$. Assuming that the latter remains unaffected by temperature, figures 4(*a*) and 4(*b*) display the intrinsic curves in the Mohr-plane relative to the strength condition (2) at *ambient* and *elevated* temperature, respectively. As it is clearly apparent from these figures, the size of strength domain delimited by the intrinsic curve is a decreasing function of temperature.

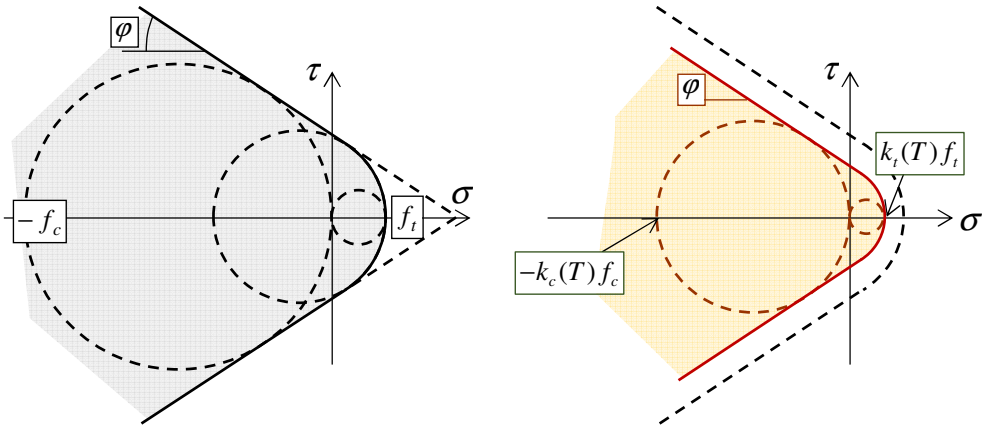

(*a*) (*b*)

Fig. 4. Intrinsic curve of plain concrete at (*a*) ambient and (*b*) elevated temperature

Looking more specifically at the particular situation of a *plane* state of stress with a zero tension cut-off condition ($f_t = 0$), the strength criterion is simply represented by a square domain in the plane of (non-zero) principal stresses, the size of which is equal to f_c (respectively $k_c(T)\,f_c$) at ambient (resp. elevated) temperature: see Fig. 5.

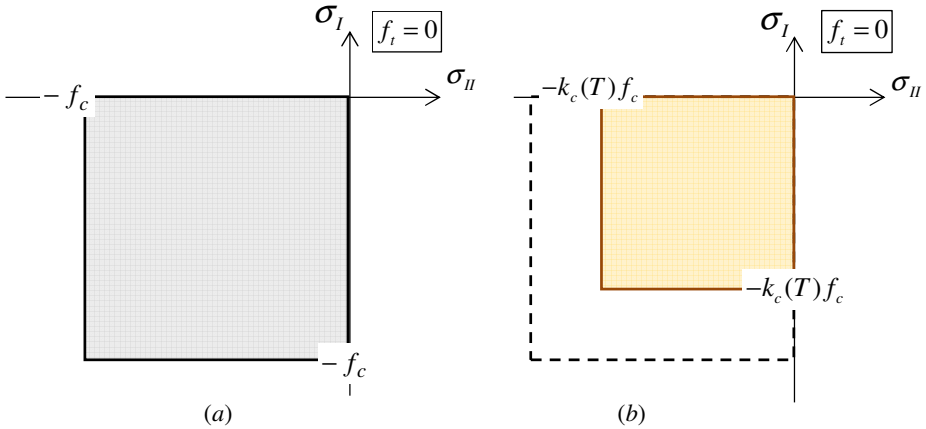

(*a*) (*b*)

Fig. 5. Strength domain of plain concrete in the plane of principal stresses at (*a*) ambient and (*b*) elevated temperature

Under such conditions, the plain concrete strength criterion can be expressed as:

$$\underline{\underline{\sigma}} \in G_c(\xi_3) \Leftrightarrow -k_c(T)\,f_c \le \sigma_I, \sigma_{II} \le 0 \Leftrightarrow \begin{cases} \sigma_{11}\sigma_{22} \ge \sigma_{12}^2 \\ \left(\sigma_{11} + k_c(T)\,f_c\right)\left(\sigma_{22} + k_c(T)\,f_c\right) \ge \sigma_{12}^2 \\ -k_c(T)\,f_c \le \sigma_{11}, \sigma_{22} \le 0 \end{cases} \tag{3}$$

Remark:

The Mohr-Coulomb strength condition (2) or (3) implicitly assumes that the uniaxial and biaxial compressive strengths of plain concrete remain the same whatever the temperature increase. However, some experiments performed on bi-axially compressed concrete specimens subjected to high temperature (Ehmet and Schneider, 1985) tend to show that the biaxial compressive strength of plain concrete is becoming larger than its uniaxial compressive strength as the temperature increases. This means that, adopting the Mohr-Coulomb failure criterion (3) with a strength reduction factor $k_c(T)$ calibrated from uniaxial compressive tests, leads to slightly underestimating the bi-axial compressive strength of plain concrete, which represents a conservative assumption.

As regards the steel reinforcements, modelled as 1D beam elements working in tension-compression only (no shear force or bending moment allowed), their resistance is characterized by the simple following inequality:

$$\left|N\right| \le N_0 = k_s(T) f_y A_s \tag{4}$$

where N denotes the axial force developed in the reinforcement and A_s its cross sectional area.

2.2. Determination of the plate strength domain $\mathcal{G}^{\hom}$ *in the space* $(\underline{\underline{N}}, \underline{\underline{M}})$

Generalizing the approach used in Pham *et al.* 2015a for constructing temperature-dependent *interaction diagrams* of a reinforced concrete beam in the (N,M)-plane, an *up-scaling* or *homogenization procedure* will once again be adopted to determine the same kind of strength condition of a reinforced concrete wall, modelled as a *periodic heterogeneous* plate. The objective is to derive a *macroscopic* plate strength domain, denoted by $\mathcal{G}^{\hom}$, to be drawn in the six-dimensional space of membrane forces $\underline{\underline{N}}$ and bending moments $\underline{\underline{M}}$. This

will be achieved by solving an *auxiliary yield design* problem defined on a representative plate volume element (Bleyer *et al.* 2018; Yang, 2018).

Figure 6 shows such a representative plate element made of plain concrete reinforced by steel bars organized in four different arrays placed along the two orthogonal directions of unit vectors $\underline{e}_\alpha$, $\alpha = 1, 2$. The plate element thickness is denoted by h, while its side is equal to the spacing a between two successive reinforcing bars, which are placed at a distance d from the plate faces. The other notations may be found in this figure. All calculations being detailed in the Appendix, the obtained results are the followings.

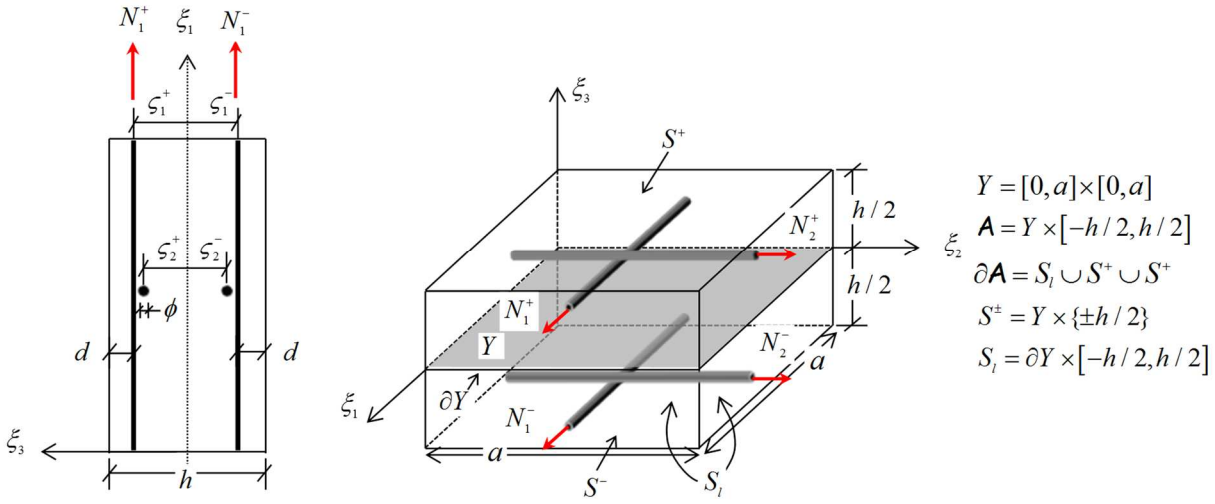

Fig. 6. Representative element of reinforced concrete plate

2.2.1. Unreinforced plain concrete plate

The macroscopic strength domain $\boldsymbol{G}_c^{\text{hom}}$ obtained from the yield design homogenization procedure may be expressed as follows:

$$(\underline{\underline{N}}, \underline{\underline{M}}) \in \boldsymbol{G}_c^{\text{hom}} \Leftrightarrow \begin{cases} N_{\alpha\beta} = \int_{-h/2}^{+h/2} \sigma_{\alpha\beta}(\xi_3)\mathrm{d}\xi_3 \ \text{ and } \ M_{\alpha\beta} = -\int_{-h/2}^{+h/2} \xi_3 \sigma_{\alpha\beta}(\xi_3)\mathrm{d}\xi_3 \\ \text{with } \sigma_{\alpha\beta}(\xi_3)\underline{e}_\alpha \otimes \underline{e}_\beta \in G_c(\xi_3) \ \ (\alpha,\beta=1,2) \end{cases} \tag{5}$$

where $G_c(\xi_3)$ is defined by (3).

2.2.2. Reinforced concrete plate

The corresponding strength domain $\mathcal{G}_{rc}^{\hom}$ is defined as:

$$(\underline{\underline{N}},\underline{\underline{M}})\in\mathcal{G}_{rc}^{\hom}\Leftrightarrow\begin{cases}\underline{\underline{N}}=\displaystyle\int_{-h/2}^{+h/2}\sigma_{\alpha\beta}(\xi_3)\underline{e}_\alpha\otimes\underline{e}_\beta\mathrm{d}\xi_3\\ \qquad+\dfrac{N_1^+ + N_1^-}{a}\underline{e}_1\otimes\underline{e}_1+\dfrac{N_2^+ + N_2^-}{a}\underline{e}_2\otimes\underline{e}_2\\ \underline{\underline{M}}=-\displaystyle\int_{-h/2}^{+h/2}\xi_3\sigma_{\alpha\beta}(\xi_3)\underline{e}_\alpha\otimes\underline{e}_\beta\mathrm{d}\xi_3\\ \qquad-\dfrac{\zeta_1^+N_1^+ + \zeta_1^-N_1^-}{a}\underline{e}_1\otimes\underline{e}_1-\dfrac{\zeta_2^+N_2^+ + \zeta_2^-N_2^-}{a}\underline{e}_2\otimes\underline{e}_2\\ \text{with }\sigma_{\alpha\beta}(\xi_3)\underline{e}_\alpha\otimes\underline{e}_\beta\in G_c(\xi_3)\text{ and }\left|N_\alpha^\pm\right|\le N_0(\zeta_\alpha^\pm)=k_s\left(T(\zeta_\alpha^\pm)\right)f_yA_s\end{cases}\tag{6}$$

where $N_\alpha^\pm$ is the axial force in the steel bar placed along the α-direction in the plane $\xi_3 = \zeta_\alpha^\pm$ (see Fig. 6).

The latter macroscopic strength condition (6) can also be formally written as a *Minkowski* sum[1]:

$$\mathcal{G}_{rc}^{\hom}=\mathcal{G}_c^{\hom}\oplus\mathcal{G}_r^{\hom}\tag{7}$$

with:

$$(\underline{\underline{N}},\underline{\underline{M}})\in\mathcal{G}_r^{\hom}\Leftrightarrow\begin{cases}\underline{\underline{N}}=\dfrac{N_1^+ + N_1^-}{a}\underline{e}_1\otimes\underline{e}_1+\dfrac{N_2^+ + N_2^-}{a}\underline{e}_2\otimes\underline{e}_2\\ \underline{\underline{M}}=-\dfrac{\zeta_1^+N_1^+ + \zeta_1^-N_1^-}{a}\underline{e}_1\otimes\underline{e}_1-\dfrac{\zeta_2^+N_2^+ + \zeta_2^-N_2^-}{a}\underline{e}_2\otimes\underline{e}_2\\ \text{with }\left|N_\alpha^\pm\right|\le N_0(\zeta_\alpha^\pm)=k_s\left(T(\zeta_\alpha^\pm)\right)f_yA_s\end{cases}\tag{8}$$

Remarks.

[1] $A\oplus B=\{a+b;\,a\in A,b\in B\}$

a. Eq. (7) clearly demonstrates that the incorporation of steel bars in the plain concrete material always leads to a significant improvement of the plate strength properties, since we obviously have the following inclusion relationship:

$$\mathcal{G}_c^{\hom} \subset \mathcal{G}_{rc}^{\hom} = \mathcal{G}_c^{\hom} \oplus \mathcal{G}_r^{\hom} \tag{9}$$

b. From a general viewpoint, the macroscopic strength condition of the wall, modelled as a plate, should involve not only the tensors of membrane forces and bending moments, but also the vector of shear forces $\underline{V}$. The fact that such shear forces are not apparent in the previous formulation, does not mean that they can be neglected, but on the contrary that the plate is assumed to exhibit an *infinite* resistance towards these shear forces. This assumption proves to be valid in the case of sufficiently "thin" plates, such as high-rise panels, the thickness of which h is very small when compared to the height H (in practice, h / H may vary from 0.15 m / 14 m to 0.15 m / 8 m, so ~ $1\% \rightarrow 2\%$).

3. NUMERICAL APPROXIMATION (Yang, 2018; Bleyer and de Buhan, 2016; de Buhan *et al.* 2017)

Looking forward to employing the above macroscopic strength criteria in a finite element-based yield design calculation, a formulation of these criteria in terms of non-linear, and more specifically conic, constraints will now be presented in the form of a lower-bound approximation. Since more details may be found in Yang, 2018; Bleyer and de Buhan, 2016; or de Buhan *et al.* 2017, a brief presentation of the method for deriving such a lower bond approximation will be made in this section.

A lower-bound approximation to $\mathcal{G}_{rc}^{\hom}$ is obtained by considering *piecewise constant* plane stress fields along the thickness direction of the concrete material. More precisely, dividing the plate thickness into n superposed layers:

$$\left[-h/2,+h/2\right]=\bigcup_{k=1}^{k=n}\left[t_{k-1},t_k\right] \text{ with } t_0=-h/2 \text{ and } t_n=+h/2 \tag{10}$$

the plane stress field is supposed to be *constant* in each layer:

$$k=1...n,\ \xi_3\in\left[t_{k-1},t_k\right]:\ \underline{\underline{\sigma}}_k=\sigma_{\alpha\beta}^k\underline{e}_\alpha\otimes\underline{e}_\beta \tag{11}$$

so that the membrane forces and bending moments equilibrated by such a piecewise constant stress field are:

$$\begin{aligned} N_{\alpha\beta}&=\int_{-h/2}^{+h/2}\sigma_{\alpha\beta}(\xi_3)\mathrm{d}\xi_3=\sum_{k=1}^{n}(t_k-t_{k-1})\sigma_{\alpha\beta}^k \\ M_{\alpha\beta}&=-\int_{-h/2}^{+h/2}\xi_3\sigma_{\alpha\beta}(\xi_3)\mathrm{d}\xi_3=-\sum_{k=1}^{n}\frac{(t_k^2-t_{k-1}^2)}{2}\sigma_{\alpha\beta}^k \end{aligned} \tag{12}$$

On the other hand, this piecewise constant stress field must comply with the concrete strength condition (3) in each layer. Since the strength domain $G_c(T(\xi_3))$ is a *decreasing* function of the temperature T, and then an *increasing* function of ξ_3 (Fig. 4), this condition is satisfied at any point of the k^{th} layer if it is satisfied at the *bottom* of this layer:

$$\underline{\underline{\sigma}}^k\in G_c\left(T(t_{k-1})\right)\subseteq G_c\left(T(\xi_3\in\left[t_{k-1},t_k\right])\right) \tag{13}$$

Finally, according to the static approach of yield design, a *lower-bound* estimate of $\mathbb{G}_c^{\text{hom}}$, denoted by $\mathbb{G}_c^{\text{LB}}$, may be defined as:

$$\mathbb{G}_c^{\text{hom}}\supseteq\mathbb{G}_c^{\text{LB}}=\left\{\begin{array}{c}(\underline{\underline{N}},\underline{\underline{M}})\ ;\quad \exists\underline{\underline{\sigma}}_k,k=1...n \\ \underline{\underline{N}}=\sum_{k=1}^{n}(t_k-t_{k-1})\underline{\underline{\sigma}}_k\ ,\ \underline{\underline{M}}=-\sum_{k=1}^{n}\frac{(t_k^2-t_{k-1}^2)}{2}\underline{\underline{\sigma}}_k \\ \underline{\underline{\sigma}}_k\in G_c\left(T(t_{k-1})\right)\end{array}\right\} \tag{14}$$

and a *lower-bound* estimate of $\mathbb{G}_{rc}^{\text{hom}}$ is given by:

$$\mathcal{G}_{rc}^{\hom} \supseteq \mathcal{G}_{rc}^{\mathrm{LB}} = \mathcal{G}_{c}^{\mathrm{LB}} \oplus \mathcal{G}_{r}^{\hom} \tag{15}$$

It can be easily shown that this lower-bound estimate is converging to the exact strength condition as the number of layers tends to infinity:

$$\lim_{n\to\infty} \mathcal{G}_{rc}^{\mathrm{LB}} = \mathcal{G}_{rc}^{\hom} \tag{16}$$

4. *STEP N°3*: STABILITY ANALYSIS OF THE WALL IN ITS DEFORMED CONFIGURATION - A YIELD DESIGN FINITE ELEMENT APPROACH

The third and final step of the general design procedure outlined in Fig. 2 will now be implemented. It consists of evaluating the stability of the entire wall, modelled as a plate in its deformed configuration obtained as the output result of *step n°1*, accounting for the reduced strength properties at any point of the wall established in *step n°2*. It is based on the yield design theory of plates and the finite element implementation of the static approach of this theory, for which more details are to be found in Yang, 2018; Bleyer and de Buhan, 2016.

4.1. Problem statement

According to the yield design theory applied to the stability of the high-rise wall under the joint action of gravity and thermal loadings, the sole *mechanical loading parameter* involved in the analysis is the self-weight w of the wall per unit area, since high-rise walls are non-bearing structures[2]. The stability of this wall is thus ensured as far as w is lower than or equal to its *ultimate value* w^+ defined as follows:

$$\text{wall stability} \Leftrightarrow w \leq w^+ = \sup\left\{ w \ ; \exists (\underline{\underline{N}}, \underline{\underline{M}}) \text{ s.t. } \begin{array}{l} (\underline{\underline{N}}, \underline{\underline{M}}) \text{ S.A. with } w \\ (\underline{\underline{N}}, \underline{\underline{M}})(x_1, x_2) \in \mathcal{G}_{rc}^{\hom} \end{array} \right\} \tag{17}$$

The non-dimensional coefficient:

[2] The present approach may however be easily extended to other loading conditions, such as transversal loads (wind) or vertical surcharges (multi-storey buildings).

$$\lambda^+ = \frac{w^+}{w} \tag{18}$$

may be called the *stability factor* of the wall.

It should be recalled that, in the above general definition, the *statically admissible* (S.A.) generalized stress fields $(\underline{\underline{N}}, \underline{\underline{M}})$ must satisfy the *equilibrium equations* to be written not on the *initial plane configuration* of the plate, but on the *deformed configuration* of the wall, modelled as a *slightly curved plate* or *shallow shell*, which would therefore necessitate the use of differential geometry of surfaces.

In order to circumvent such theoretical difficulties while facilitating at the same time the numerical treatment of the above yield design problem defined by (17) in the framework of the finite element method, a discretized approximation of the shell or curved plate geometry is proposed.

4.2. Finite element formulation for the lower bound static approach

The curved surface of the deformed wall is thus approximated by an assembly of planar triangular facets connected to each other along their edges as shown in Fig. 7 and which can also be regarded as *plate-type finite elements*. Following the approach developed in Bleyer and de Buhan, 2014, the numerical resolution of the static approach of yield design is performed by considering piecewise continuous membrane-shear forces and bending moment distributions, separated by statically admissible discontinuities across adjoining plate elements. A linear interpolation is assumed for the tensor of membrane forces $\underline{\underline{N}}$ and vector of shear forces $\underline{V}$ inside each triangular plate element, whereas a quadratic variation is adopted for the tensor of bending moments $\underline{\underline{M}}$.

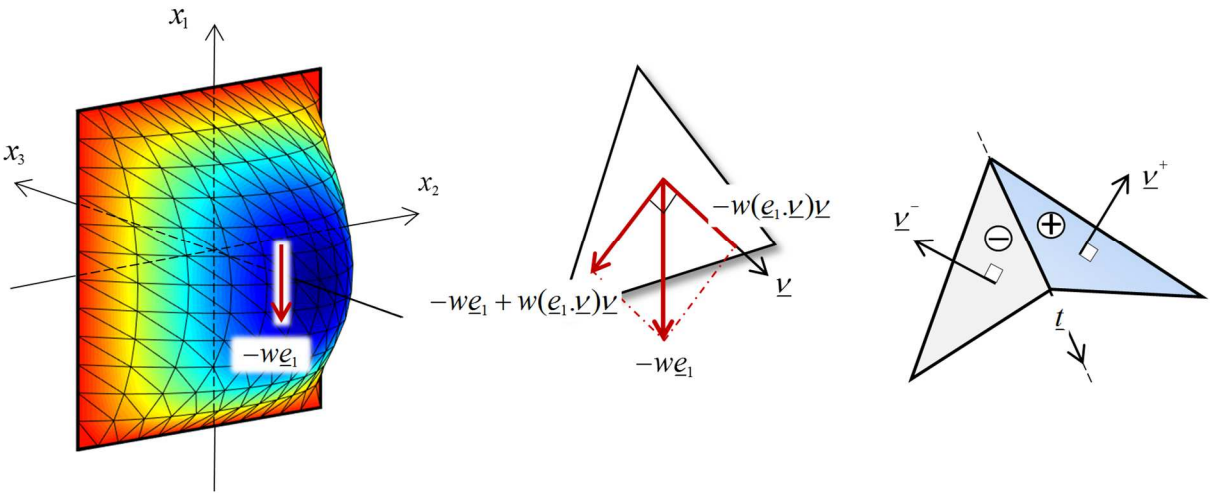

Fig. 7. Discretization of the geometry of a deformed plate into triangular plane facets

The local equilibrium equations at any point of any such planar plate elements are:

$$\mathrm{div}\underline{\underline{N}} - w\underline{e}_1 + w(\underline{e}_1.\underline{\nu})\underline{\nu} = 0 \ , \ \mathrm{div}\underline{V} + w(\underline{e}_1.\underline{\nu}) = 0 \ , \ \mathrm{div}\underline{\underline{M}} + \underline{V} = 0 \tag{19}$$

where $\underline{\nu}$ is the unit normal to the plate element (Fig. 7).

These equations must be completed by jump relationships across a common edge of unit tangent $\underline{t}$ between two adjacent plate elements as those shown in Fig. 6, where $\underline{n}^{\pm} = \underline{t} \wedge \underline{\nu}^{\pm}$:

$$\begin{aligned} \left[\underline{\underline{N}}.\underline{n} + (\underline{V}.\underline{n})\underline{\nu}\right] &= \underline{\underline{N}}^+.\underline{n}^+ + (\underline{V}^+.\underline{n}^+)\underline{\nu}^+ - \underline{\underline{N}}^-.\underline{n}^- - (\underline{V}^-.\underline{n}^-)\underline{\nu}^- = 0 \\ \left[\underline{\underline{M}}.\underline{n}\right] &= \underline{\underline{M}}^+.\underline{n}^+ - \underline{\underline{M}}^-.\underline{n}^- = 0 \end{aligned} \tag{20}$$

and finally appropriate static conditions must be prescribed along the boundaries of the wall.

All the above equilibrium conditions ensure that the generalized stress fields $(\underline{\underline{N}}, \underline{\underline{M}})$ defined at any point of the discretized wall are *statically admissible* (S.A.) with the loading parameter w. Making use of the different interpolations of these fields inside the plate finite elements, it can be shown that all these conditions may be expressed through the following global linear relationship:

$$\mathbf{H\Sigma} + \lambda \mathbf{F}_0 = \mathbf{0} \tag{21}$$

where Σ denotes the vector collecting all the static variables defining the discretized stress fields, while $\mathbf{F}_0$ is the vector of external forces associated with the wall self-weight w and λ is a variable multiplicative coefficient.

Making use of definitions (17) and (18), the following *lower bound estimate* of the wall stability factor is finally obtained as a result of the above-described finite element discretization:

$$\lambda^+ \geq \lambda^{\mathrm{LB}} = \sup \left\{ \lambda \text{ s.t. } \begin{array}{l} \mathbf{H\Sigma} + \lambda \mathbf{F}_0 = \mathbf{0} \\ (N^c_{\alpha\beta}, M^c_{\alpha\beta}) \in \mathcal{G}^{\mathrm{LB}}_{rc}, \ \forall c = 1,...,N_c N_E \end{array} \right\} \tag{22}$$

where the superscript c spans all the points where the strength condition attached to $\mathcal{G}_{rc}^{\mathrm{LB}}$ must be verified as discussed in Bleyer and de Buhan, 2014. N_c is the number of checkpoints inside each plate element and N_E the number of elements.

Since the (lower bound) strength condition relating to G_{rc}^{LB} may be expressed by means of *second order conic constraints* (see (3)), the determination of λ^{LB} is ultimately resorting to a *second order conic programming* (SOCP) problem, which can be efficiently treated with dedicated solvers Mosek optimization software, 2020.

5. IMPLEMENTATION OF THE THREE-STEP DESIGN PROCEDURE AND PRESENTATION OF RESULTS

For illustrative purpose, the three-step design procedure presented in Fig. 2 is now implemented for some typical configurations of high-rise walls. This will help quantify more precisely the negative effect of high temperature increase on the stability of such slender structures, expressed through the "*P-δ effect*" (*step n° 1*) combined with the decrease of the

local material strength properties (*step n° 2*), which finally leads to the decrease of the global stability factor of the whole structure (*step n° 3*).

5.1. General input data and heat transfer analysis

Numerical examples are conducted on a rectangular wall of thickness $h = 15$ cm, height $H = 12$ m and width $L = 12$ m. It is made of a homogenous plain concrete with siliceous aggregates, exhibiting a compressive strength $f_c = 36$ MPa, a Young's modulus $E = 21.66$ GPa and a Poisson's ratio $\nu = 0.2$ at ambient temperature (20°C), the tensile strength f_t of concrete being neglected.

Referring to the notations of Fig. 6, this wall is reinforced by 2 layers of ∅6mm hot rolled steel reinforcing bars of yield strength $f_y = 500$ MPa. These steel bars, equally spaced by 100 mm, are arranged in two orthogonal arrays with 30 mm of concrete cover at top and bottom.

The wall is simply supported along the top and bottom edges and stress-free along the vertical sides as sketched in Fig. 8. The weight of the wall per unit area (self-weight density) is equal to $w = 3.75$ kN/m^2. In the following analysis, the Poisson coefficient ν is considered as a constant with respect to temperature changes, whereas other stiffness and strength properties of both concrete and steel are considered to be temperature dependent according to experimental curves available in Eurocode 2-Part 1-2 (EN1992-1-2, 2004).

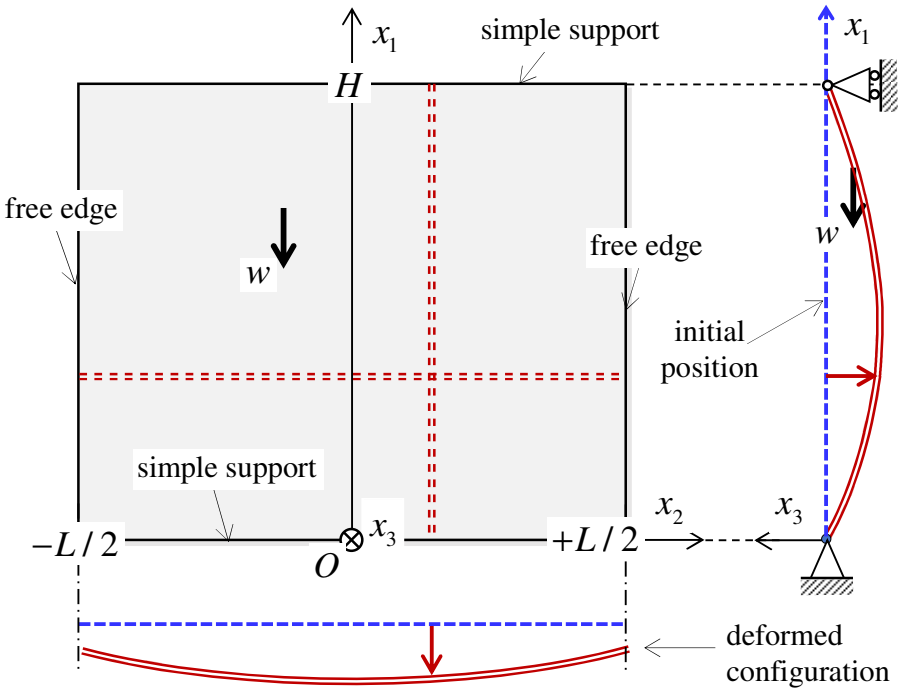

Fig. 8. Front, top and side views of a fire-exposed wall modelled as a rectangular plate

Assuming that the wall is subjected to an ISO 834 fire (EN1991-1-2, 2002) on one face, a preliminary heat transfer analysis is firstly carried out using the SAFIR computer program (Franssen, 2005) to evaluate the temperature increase across the wall thickness for different fire durations (see for example Fig. 9). The concrete of EN 1992-1-2, 2004 according to the French National Appendix (NF EN 1992-1-2/NA, 2007) with some thermal properties that vary with temperature has been used. Moreover, since the diameter of steel bars is small, their temperature could be considered as corresponding to that of the concrete located at the same position.

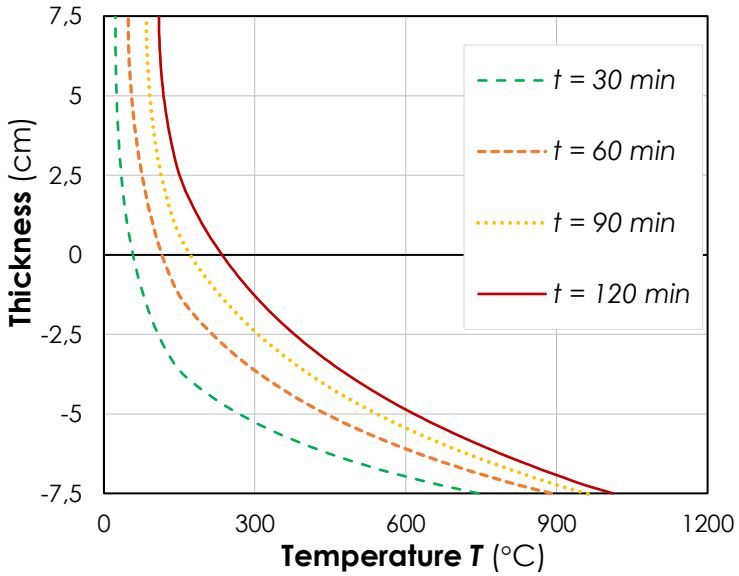

Fig. 9. Examples of temperature profile across the wall thickness as a function of the fire exposure time

5.2. Implementation of step n° 1

As described in the general procedure (Fig. 2), the geometric configuration of the reinforced concrete wall subject to fire (*step n° 1*) on which the yield design approach is to be performed, is not known *a priori*. Such deformed configurations of the wall could be determined by the use of the *von Karman* (*VK*) and *linearized Love-Kirchhoff* (*LK*) models (see Yang, 2018, for more details). For illustrative purpose, figure 10 displays the variations with H of the maximum deflection of a wall calculated according to these two plate models, showing that the *VK*-computed deflections are significantly greater than the ones based upon the *LK* model, which highlights the "*P-δ effect*" captured by the *von Karman* model (see Yang, 2018, for more details).

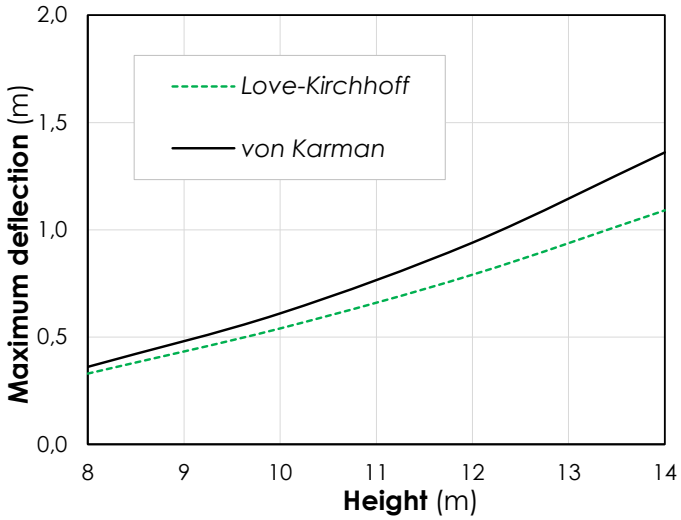

Fig. 10. Example of calculated maximum deflection of a wall as a function of its height for 90 min of fire exposure

5.3. Implementation of step n° 2

As regards *step n° 2*, figure 11 below shows different numerical lower bound approximations to the cross-sectional view of $\mathcal{G}_{rc}^{\hom}$ in the (N_{11}-M_{11})-plane[3] at ambient temperature ($T = 20°C$). Note that the boundary of this cross-section is nothing but the interaction diagram of the reinforced concrete plate subject to the combined action of axial force N_{11} and bending moment M_{11}, all the other components being kept equal to zero. As can be seen in this figure, the numerical lower approximations calculated from the above discretized formulations, provide a fairly accurate bracketing of the exact macroscopic strength domain as soon as the discretization number is equal to $n = 11$.

[3] $N_{\alpha\beta} = M_{\alpha\beta} = 0$ if $(\alpha,\beta) \neq (1,1)$

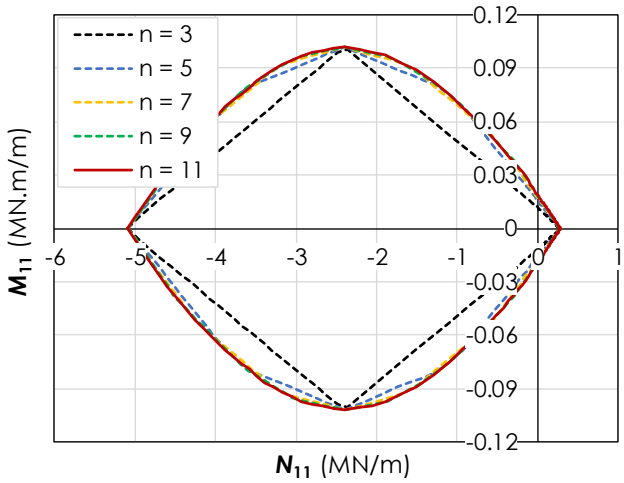

Fig. 11. Numerical lower bound approximations to the interaction diagram of reinforced concrete wall at ambient temperature in the (N_{11}-M_{11})-plane

Due to the absence of any temperature gradient, the plain concrete strength condition is homogeneous. This homogeneity as well as the symmetric arrangement of the reinforcements with respect to the plate middle-plane, explain the fact that the numerical approximations are all symmetric with respect to the N_{11}-axis. This is of course no longer true in the presence of any temperature gradient, as it is obviously apparent in Fig. 12. Furthermore, the correlative strength reduction of the heated reinforced concrete plate observed in the same figure, clearly confirms the results previously obtained in the case of a reinforced concrete beam section (Pham *et al.* 2015a).

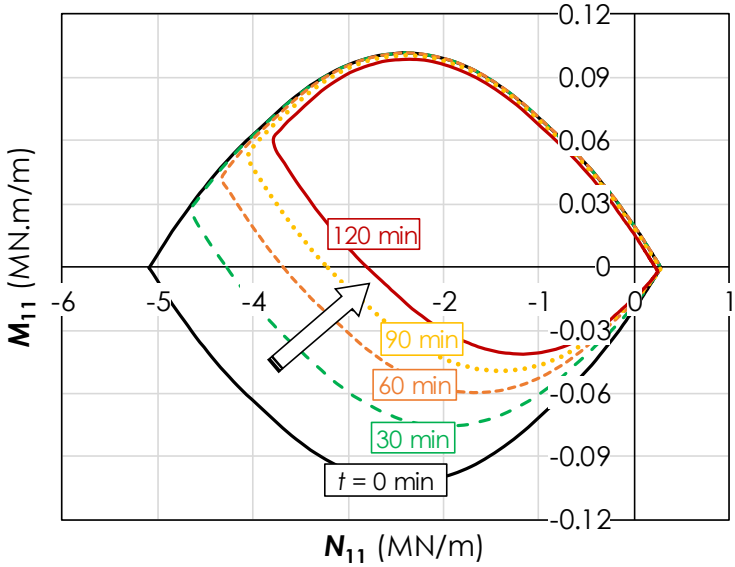

Fig. 12. Interaction diagram in the (N_{11}-M_{11})-plane as a function of the fire exposure time

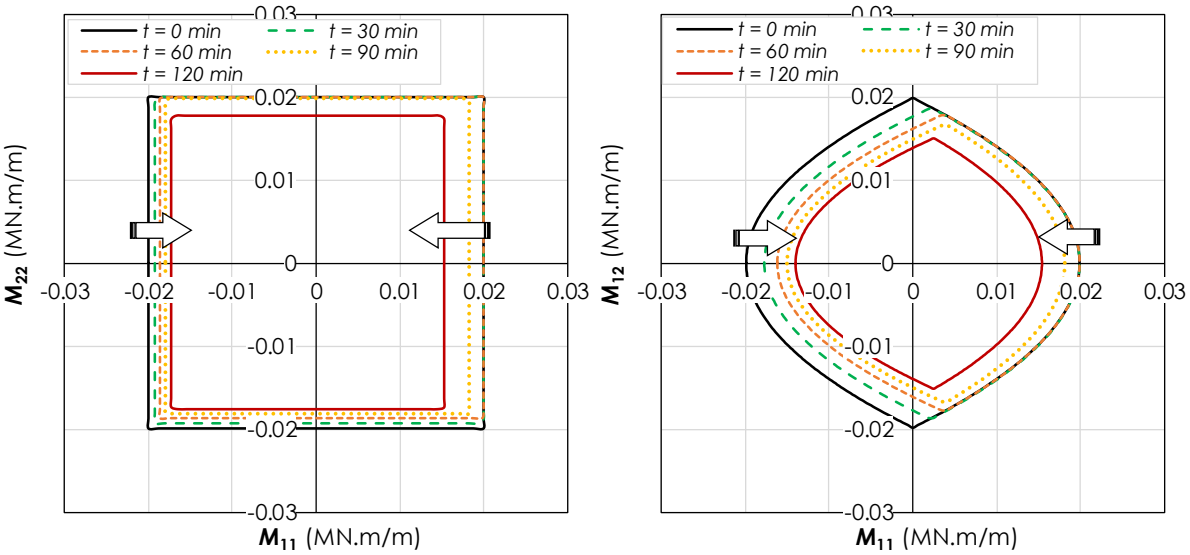

Fig. 13. Representation of the plate macroscopic strength condition in the case of (*a*) biaxial bending and (*b*) combined bending/torsion

Two other representations of the macroscopic strength domain and its evolution as a function of the fire exposure time are shown in Fig. 13. Figure 13(*a*) displays the square shaped domain in the (M_{11}-M_{22})-plane corresponding to a plate under biaxial bending, while figure 13(*b*) corresponds to the situation of a plate under combined bending and torsion. A significant strength reduction with the increase of temperature is always observed, according to the general property:

$$\forall t_2 > t_1 \geq 0 : \mathcal{G}_{rc}^{\hom}(t_2) \subseteq \mathcal{G}_{rc}^{\hom}(t_1) \tag{23}$$

5.4. Implementation of step n° 3

Relying on the deformed geometry of the wall calculated from section *5.2* (*step n°1*) and the reduced strength capacities at any point of the wall obtained as a result of section *5.3* (*step n°2*), the results of the final step (*step n° 3*) dealing with the lower bound static approach of the yield design-based analysis of the whole structure are reported in Fig. 14. This figure clearly shows that the increase of fire exposure duration results in a lower stability factor of the wall. Failure occurs when the value of this stability factor reduces to 1. In the case of this

example, it indicates that the rectangular wall of height H = 12 m and width L = 12 m will not resist more than 112 min in fire.

Besides, it has been shown in Fig. 10 that the *von Karman* computed deflections are always greater than the ones based upon the classical *Love-Kirchhoff* model, which highlights the "*P-δ effect*" captured by the *von Karman* model (see also Yang, 2018 for more details). In such a case, it may be interesting here to compare the stability factors obtained from the yield design approach on the deformed configurations of the wall calculated according to the two plate models (see Fig. 14).

Once again, it is confirmed that performing the yield design approach on the deformed configuration obtained with *von-Karman* model always leads to a lower stability factor than the one with *Love-Kirchhoff* model. In the present example, the stability of the wall is ensured until 180 min of fire with the *Love-Kirchhoff* model, while the wall has already reached its failure at 112 min with the *von-Karman* model. Consequently, evaluating the fire resistance of such a high-rise wall with the classical *Love-Kirchhoff* model may lead to the unsafe results. In the following, the deformed configurations of the wall will be obtained with the *VK* plate model.

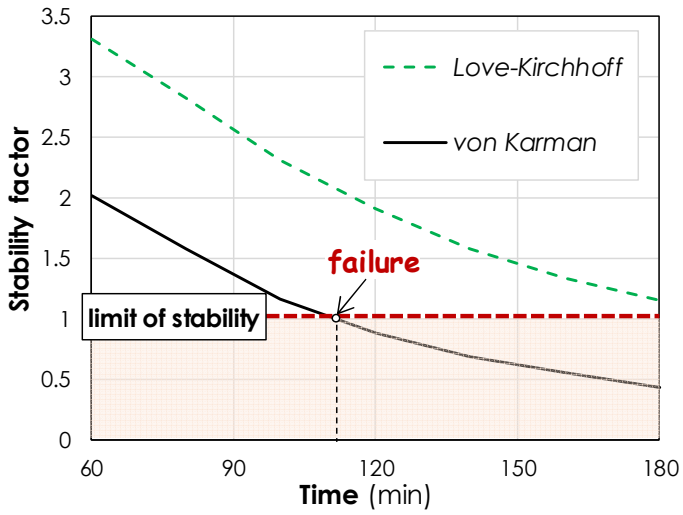

Fig. 14. Evolution of stability factors of the wall as function of fire exposure

5.5. Influence of the wall height

As already observed for instance in Pham *et al.* 2015b or recently Yang, 2018, the higher is the wall, the larger are the out-of-plane displacements (deflections). In this context, the main objective of this section is to determine at which height failure of the wall will occur for a given fire exposure.

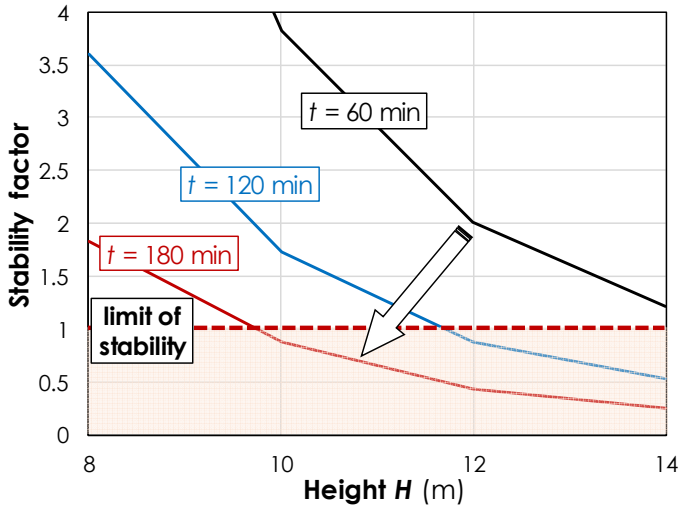

Fig. 15. Evolutions of stability factors of the wall of width L = 12 m as function of its height H for different fire exposures

A simple practical method may be found in Fig. 15, which shows for example the evolutions of wall (of fixed width L = 12 m) stability factor as a function of its height H, for different fire exposures of 60, 120 and 180 min. Focussing for example on the given fire exposure of 180 min, it is shown that the corresponding stability factor curve intersects the limit of stability line for a height close to 9.5 m. It means that the height of the wall should not exceed 9.5°m if a fire resistance of 180 min is required. On the contrary, this wall could be higher than 14 m if only 60 min of fire resistance is required.

5.6. Influence of the wall width

Regarding the width of the wall, it seems that the variation of the wall width has no similar effects on the global stability as that of the wall height: see for instance Fig. 16 presenting the evolutions of stability factors of the wall of height H = 12 m, as function of its width L for different fire exposures. It is shown that the fire resistances of 120 and 180 min could not be satisfied by only modifying the wall width (but it may be satisfied by reducing the wall height as shown in the above section) while for 100 min for example, the required fire resistance may be satisfied for a width comprised between 5 and 18 m.

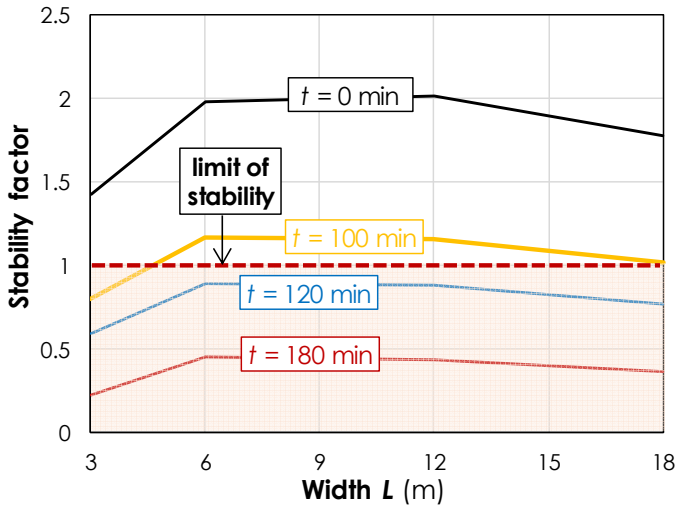

Fig. 16. Evolutions of stability factors of the wall of height H = 12 m as function of its width L for different fire exposures

5.7. Influence of the lateral boundary conditions

In order to investigate the influence of the lateral boundary conditions on the stability factor additional numerical simulations have been conducted on a wall simply supported along its four edges, the other characteristics being identical with those of the first wall simply supported along the top and bottom edges and stress-free along the vertical sides, as in the previous example. The evolution of the corresponding stability factors of the two walls as functions of fire exposure are reported in Fig. 17.

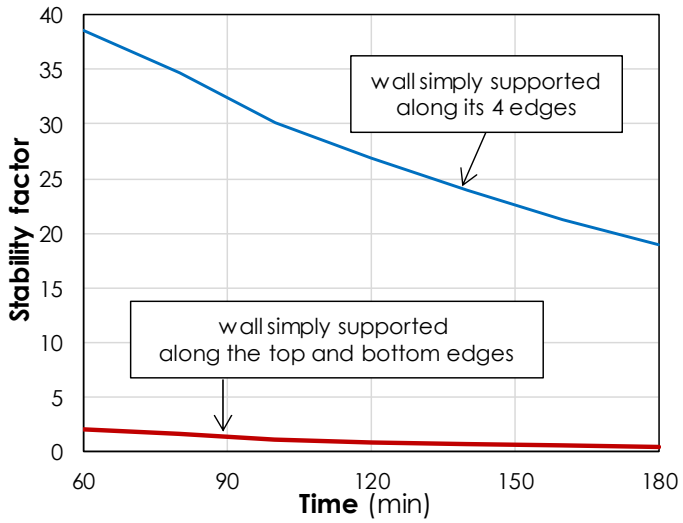

Fig. 17. Comparison of the stability factors of the wall simply supported along its four sides with those of the wall simply supported along the top and bottom edges and stress-free along the vertical sides

It can be immediately seen that the corresponding stability factor of the second wall simply supported along its fours edges is much higher than the stability factor of the first wall, simply supported along the top and bottom edges only, which means that the stability of the wall is ensured by a large margin. This should of course be attributed to the stabilizing effects of the lateral boundary conditions which:

- tend to limit the out-of-plane displacements of the wall and then the amplitude of its change of geometry (see Yang, 2018 for more details);
- while at the same time quite significantly improve the global stability of the wall by prescribing zero out-of-plane displacements along the lateral edges.

6. CONCLUSION

This contribution has laid the theoretical as well as computational foundations for a rational failure design method of high-rise panels subject to fire loading. It relies on the implementation of the yield design theory on two different levels:

- at the local scale through the determination of a macroscopic strength condition for the wall element, expressed in terms of membrane forces and bending moments,

depending on the strength parameters of the constituent materials (plain concrete and steel reinforcement) and on the fire-generated temperature profile;

- at the structural level by modelling the previously determined deformed wall as a shallow shell (or curves plate), the overall stability of which is investigated by means of the lower bound method of yield design making use of a finite element discretization of the wall into plane triangular facets.

The whole computational procedure has been applied to a typical configuration of high-rise reinforced concrete panel subject to a normalized fire loading. As could be anticipated, the factor of stability of the wall is strongly decreasing with the wall height as well as the fire exposure. But the most important result concerns the crucial role played by the boundary conditions prescribed along the vertical lateral sides of the wall. Indeed, in the case of stress-free lateral sides, the stability factor of the wall may be lower than one as soon as the wall height is larger than 12 m and/or the fire duration longer than 120 min.

On the contrary, in the case of walls simply supported along their vertical edges, which is the most frequently encountered situation, the corresponding evaluations of the stability factors are several tens of times higher than in the previous case, thereby suggesting that the stability of the wall is always ensured with a sufficient safety margin. This preliminary conclusion should however be questioned for the following reasons:

a) The lateral supporting columns on both sides of the wall are supposed to remain un-deformed, which is not a necessarily valid assumption, since these columns may suffer the same kind of thermal deformations as the wall itself.
b) High rise walls are often built from the vertical assemblage of rectangular panels connected to each other by means of male-female notches, so that the wall can no longer be modelled as a continuous plate or shell. The previous analysis should

therefore be reconsidered, taking the absence of bending stiffness and resistance of the connecting joints into account.

c) More fundamentally, the stability factor defined by Eq. (30) is calculated on the deformed geometry of the wall under the action of its *actual* self-weight w, regardless of the amplification of the wall deformations due to the increase from w to its ultimate value w^+. As a consequence, the present analysis most likely overestimates the value w^+ and thus of $\lambda^+ = w^+ / w$.

d) Finally, the above-described computational procedure could be generalized to the situation where the stability of the wall is "post-analysed", that is at the end of the fire-induced heating-cooling cycle. This may certainly require performing compressive tests on concrete/reinforcement specimens having been preliminary submitted to such a thermal cycle. It is then highly probable that the degradation of the material properties observed during the heating phase is irreversible.

The above comments provide a guideline for future works aimed at improving the present approach.

REFERENCES

Averbuch, D. (1996). Yield design of reinforced concrete structures. PhD thesis, ENPC, Paris, France [in French].

Bazant, Z. and Cedolin, L. (2010). Stability of structures: elastic, inelastic, fracture and damage theories. World Scientific.

Bleyer, J. and de Buhan, P. (2014). Lower bound static approach for the yield design of thick plates. International Journal for Numerical Methods in Engineering, 100:814-833.

Bleyer, J. and de Buhan, P. (2016). A numerical approach to the yield strength of shell structures. European Journal of Mechanics A/Solids, 59:178-194.

Bleyer, J., Pham, D. T. and de Buhan, P. (2017). Numerical yield design of high-rise reinforced concrete walls in fire conditions. Advances in Direct Methods for Materials and Structures, Springer, Cham, 143-161.

Caldas, R. B., Sousa, Jr. J. B. M. and Fakury, R. H. (2010). Interaction diagrams for reinforced concrete sections subjected to fire. Engineering Structures, 32:2832-2838.

Chen, W. F. (1982). Plasticity in reinforced concrete, New-York: Mc Graw-Hill.

de Buhan, P. and Taliercio, A. (1991). A homogenization approach to the yield strength of composite materials. European Journal of Mechanics A/Solids, 10(2):129-150.

de Buhan, P., Bleyer, J. and Hassen, G. (2017). Elastic, Plastic and Yield Design of Reinforced Structures, ISTE-Elsevier, 328 p.

Dotreppe, J. C., Franssen, J. M. and Vanderzeypen, Y. (1999). Calculation method for the design of reinforced concrete columns under fire conditions. ACI Structural Journal, 96(1):9-18.

Ehm, C. and Schneider, U. (1985). The high temperature behavior of concrete under biaxial conditions. Cement and Concrete Research, 15, 1: 27-34.

El Fatni, S. F. and Youssef, M. A. (2009). Assessing the flexural and axial behaviour of reinforced concrete members at elevated temperatures using sectional analysis. Fire Safety Journal, 44:691-703.

EN1991-1-2 (2002). Eurocode 1: actions on structures-Part 1-2: General actions. Actions on structures exposed to fire.

EN1992-1-2. Eurocode 2 (2004). Design of concrete structures-Part 1 2: General rules-structural fire design.

Franssen, J. M. (2005). SAFIR: a thermal/structural program for modeling structures under fire. Engineering Journal, 42:143–58.

Franssen, J. M. and Dotreppe, J. C. (2003). Fire tests and calculation methods for circular concrete columns. Fire Technology, 39:89-97.

Gernay, T. and Franssen, T. (2015). A plastic-damage model for concrete in fire: applications in structural fire engineering. Fire Safety Journal, 71:268–278.

Jianga, J., Chenb, L., Jiangc, S., Lic, G.-Q., Usmani, A. (2015). Fire safety assessment of super tall buildings: a case study on Shanghai Tower. Case Studies in Fire Safety, 4:28–38.

Koechlin, P. and Potapov, S. (2007). Global constitutive model for reinforced concrete plates. Journal of Engineering Mechanics, 133:257-266.

Kumar, P. and Kodur, V.K.R. (2017). Modeling the behavior of load bearing concrete walls under fire exposure. Construction and Building Materials, 154:993-1003.

Law, A. and Gillie, M. (2010). Interaction diagrams for ambient and heated concrete sections. Engineering Structures, 32:1641-1649.

Lie, T. T. and Celikkol, B. (1991). Method to calculate the fire resistance of circular reinforced concrete columns. ACI Materials Journal, 88(1):84-91.

Lie, T. T. and Irwin, R. J. (1993). Method to calculate the fire resistance of reinforced concrete columns with rectangular cross section. ACI Materials Journal, 90(1):52-60.

Marti, P. (1985). Truss models in detailing. Concrete International, 7(12):66-73.

NF EN 1992-1-2/NA (2007). Eurocode 2 - Calcul des structures en béton - Partie 1-2 : Règles générales - Calcul du comportement au feu - Annexe nationale à la NF EN 1992-1-2.

Nielsen, M. P. and Hoang, L. C. (2010). Limit Analysis and Concrete Plasticity, CRC Press, Taylor & Francis.

Pham, D. T. (2014). Yield design based analysis of high rise reinforced concrete walls in fire. PhD thesis, Paris-Est University [in French].

Pham, D. T., de Buhan, P., Florence, C., Heck, J. V. and Nguyen, H. H. (2015a). Interaction diagrams of reinforced concrete in fire: a yield design approach. Engineering Structures, 90:38-47.

Pham, D. T., de Buhan, P., Florence, C., Heck, J. V. and Nguyen, H. H. (2015b). Yield-design based of high rise concrete walls subjected to fire loading conditions. Engineering Structures, 87:153-161.

Roy, T. and Matsagar, V. (2020). Fire fragility of reinforced concrete panels under transverse out-of-plane and compressive in-plane loads. Fire Safety Journal, 113: 102976.

Salençon, J. (2013). Yield Design. Great Britain and the United States: ISTE Ltd and John Wiley and Sons, Inc.

Talamona, D and Franssen J.-M. (2005). A Quadrangular Shell Finite Element for Concrete and Steel Structures Subjected to Fire. 15(4):237-264.

The Mosek optimization software (2020). Available from http://www.mosek.com

Yang, M. (2018). Stability analysis of fire-loaded reinforced concrete walls by means of the yield design theory. PhD thesis, Paris-Est University. Paris, France [in French].

APPENDIX

Determination of the macroscopic strength domain $\mathcal{G}^{\text{hom}}$

This Appendix is devoted to the derivation of the plate *macroscopic strength domain* $\mathcal{G}^{\text{hom}}$, which can be represented in the six-dimensional space of membrane forces $\underline{\underline{N}}$ and bending moments $\underline{\underline{M}}$. In much the same way as it has been previously done for deriving its thermo-elastic behaviour (see Yang *et al.* 2021), it relies on the solution to an *auxiliary yield-design problem* defined on a representative three-dimensional reinforced concrete plate element shown in Fig. 5, with the corresponding notations.

A1. Non-reinforced concrete plate subject to a temperature gradient

A1.1. General definition

The *virtual work principle per unit area* of a square plate element of side a may be written by the following expression:

$$\forall \hat{\underline{U}} \ K.A. \text{ with } (\hat{\underline{\underline{\epsilon}}}', \hat{\underline{\underline{\chi}}}') : \quad P_e(\hat{\underline{U}}) = (1/a^2)\int_A \underline{\underline{\sigma}} : \underline{\underline{d}}(\hat{\underline{U}})\mathrm{d}A = \underline{\underline{N}} : \hat{\underline{\underline{\epsilon}}}' + \underline{\underline{M}} : \hat{\underline{\underline{\chi}}}' \tag{A.1}$$

with:

$$\underline{\underline{N}} = (1/a^2)\int_A \sigma_{\alpha\beta}\underline{e}_\alpha \otimes \underline{e}_\beta \mathrm{d}A \ \text{ and } \ \underline{\underline{M}} = -(1/a^2)\int_A \xi_3 \sigma_{\alpha\beta}\underline{e}_\alpha \otimes \underline{e}_\beta \mathrm{d}A \tag{A.2}$$

representing the *six loading parameters* of the plate element.

Under those conditions, the general definition of the *macroscopic strength domain* for the *plain concrete* plate is therefore:

$$(\underline{\underline{N}},\underline{\underline{M}}) \in \mathcal{G}_c^{\hom} \Leftrightarrow \begin{cases} \exists \underline{\underline{\sigma}} \ S.A. \text{ with } (\underline{\underline{N}},\underline{\underline{M}}) \\ \forall \underline{\xi} \in \mathcal{A}, \ \underline{\underline{\sigma}}(\underline{\xi}) \in G_c(\xi_3) \end{cases} \tag{A.3}$$

where the local strength domain of plain concrete affected by the temperature increase is defined by Eq. (2) with the tensile resistance assumed to be equal to zero: $f_t = 0$.

A1.2. Static approach using plane-stress fields

The lower bound static approach to the yield design problem defined by (A.3) is implemented through the use of *plane stress* fields depending on the coordinate ξ_3 only:

$$\underline{\underline{\sigma}}(\underline{\xi}) = \sigma_{\alpha\beta}(\xi_3)\underline{e}_\alpha \otimes \underline{e}_\beta, \ \ \alpha,\beta=1,2 \tag{A.4}$$

which automatically satisfy the equilibrium equation ($\mathrm{div}\underline{\underline{\sigma}} = 0$) and equilibrate the following tensors of membrane forces and bending moments:

$$\begin{aligned} \underline{\underline{N}} &= (1/a^2)\int_{\mathcal{A}} \sigma_{\alpha\beta}(\xi_3)\underline{e}_\alpha \otimes \underline{e}_\beta \mathrm{d}\mathcal{A} = \int_{-h/2}^{+h/2} \sigma_{\alpha\beta}(\xi_3)\underline{e}_\alpha \otimes \underline{e}_\beta \mathrm{d}\xi_3 \\ \underline{\underline{M}} &= -(1/a^2)\int_{\mathcal{A}} \xi_3\sigma_{\alpha\beta}\underline{e}_\alpha \otimes \underline{e}_\beta \mathrm{d}\mathcal{A} = -\int_{-h/2}^{+h/2} \xi_3\sigma_{\alpha\beta}(\xi_3)\underline{e}_\alpha \otimes \underline{e}_\beta \mathrm{d}\xi_3 \end{aligned} \tag{A.5}$$

Hence the following *lower bound* estimate:

$$(\underline{\underline{N}},\underline{\underline{M}}) \in \mathcal{G}_c^{\mathrm{LB}} \subseteq \mathcal{G}_c^{\hom} \Leftrightarrow \begin{cases} N_{\alpha\beta} = \int_{-h/2}^{+h/2} \sigma_{\alpha\beta}(\xi_3)\mathrm{d}\xi_3 \ \text{ and } \ M_{\alpha\beta} = -\int_{-h/2}^{+h/2} \xi_3\sigma_{\alpha\beta}(\xi_3)\mathrm{d}\xi_3 \\ \text{with } \sigma_{\alpha\beta}(\xi_3)\underline{e}_\alpha \otimes \underline{e}_\beta \in G_c(\xi_3) \ \ (\alpha,\beta=1,2) \end{cases} \tag{A.6}$$

It can be observed that the plain concrete strength condition may be formulated as in Eq. (3):

$$\underline{\underline{\sigma}} \in G_c(\xi_3) \Leftrightarrow -k_c(T)f_c \le \sigma_I, \sigma_{II} \le 0 \Leftrightarrow \begin{cases} \sigma_{11}\sigma_{22} \ge \sigma_{12}^2 \\ \left(\sigma_{11} + k_c(T)f_c\right)\left(\sigma_{22} + k_c(T)f_c\right) \ge \sigma_{12}^2 \\ -k_c(T)f_c \le \sigma_{11}, \sigma_{22} \le 0 \end{cases} \tag{A.7}$$

A2. Case of the reinforced concrete plate

The result, given by Eqs. (6) or (7) and (8), may be proved without any loss of generality, by assuming that the plain concrete plate element is reinforced by one single steel bar placed for example along the ξ_1-axis (Fig. A1). The bar is modelled as a three dimensional cylindrical volume $\mathcal{A}_r$ of cross sectional area A_s placed at a distance $\xi_3 = \zeta$ from the mid-plane and made of a steel of uniaxial tensile-compressive resistance equal to $f_y(\xi_3 = \zeta)$. In this case the macroscopic strength domain of the reinforced plate is:

$$\mathcal{G}_{rc}^{\hom} = \mathcal{G}_{c}^{\hom} \oplus \mathcal{G}_{r}^{\hom} \tag{A.8}$$

with:

$$(\underline{\underline{N}}, \underline{\underline{M}}) \in \mathcal{G}_{r}^{\hom} \Leftrightarrow \begin{cases} \underline{\underline{N}} = \dfrac{N}{a} \underline{e}_1 \otimes \underline{e}_1, \quad \underline{\underline{M}} = -\dfrac{\zeta N}{a} \underline{e}_1 \otimes \underline{e}_1 \\ \text{with} \quad |N| \le N_0(\zeta) = f_y(\zeta) A_s \end{cases} \tag{A.9}$$

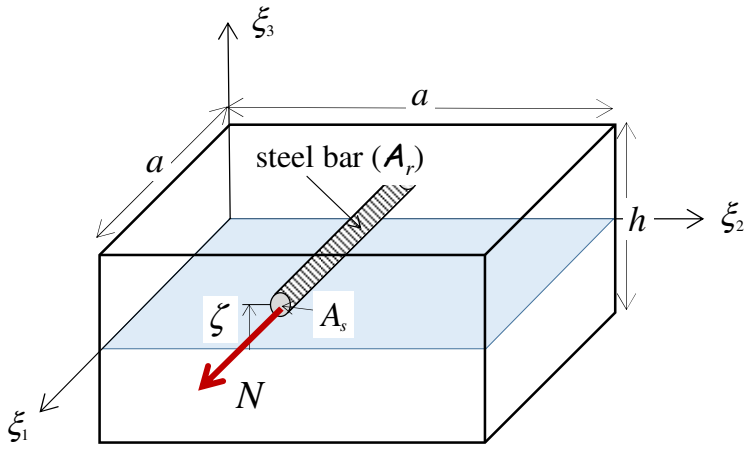

Fig. A1. Representative plain concrete volume element reinforced along the ξ_1-axis

The *lower bound static approach* of yield design is first employed, making use of stress fields of the form:

$$\underline{\underline{\sigma}}^{rc}(\underline{\xi}) = \underline{\underline{\sigma}}^{c}(\underline{\xi}) + \underline{\underline{\sigma}}^{r}(\underline{\xi}) \text{ with } \underline{\underline{\sigma}}^{r}(\underline{\xi}) = \begin{cases} \sigma^{r}\,\underline{e}_1 \otimes \underline{e}_1 & \text{if } \underline{\xi} \in \mathcal{A}_r \\ 0 & \text{if } \underline{\xi} \notin \mathcal{A}_r \end{cases} \tag{A.10}$$

where σ^r is a *constant* uniaxial stress and $\underline{\underline{\sigma}}^{c}$ a *statically admissible* stress field in equilibrium with the following loading parameters:

$$N^{c}_{\alpha\beta} = (1/a^2)\int_{\mathcal{A}} \sigma^{c}_{\alpha\beta}(\underline{\xi})\ \mathrm{d}\mathcal{A}\,,\ M^{c}_{\alpha\beta} = -(1/a^2)\int_{\mathcal{A}} \xi_3 \sigma^{c}_{\alpha\beta}(\underline{\xi})\mathrm{d}\mathcal{A} \tag{A.11}$$

Furthermore, one can notice that the stress field $\underline{\underline{\sigma}}^{r}$ is also *statically admissible* in the specified loading mode, and in equilibrium with:

$$\begin{aligned} \underline{\underline{N}}^{r} &= (1/a^2)\int_{\mathcal{A}_r} \sigma^{r}\,\underline{e}_1 \otimes \underline{e}_1\ \mathrm{d}\mathcal{A} \\ &= \sigma^{r}\left|\mathcal{A}_r\right|/a^2\,\underline{e}_1 \otimes \underline{e}_1 = \sigma^{r}A_s/a\ \underline{e}_1 \otimes \underline{e}_1 = N/a\ \underline{e}_1 \otimes \underline{e}_1 \\ \underline{\underline{M}}^{r} &= -(1/a^2)\int_{\mathcal{A}_r} \xi_3 \sigma^{r}\,\underline{e}_1 \otimes \underline{e}_1\ \mathrm{d}\mathcal{A} \\ &= -\sigma^{r}\left|\mathcal{A}_r\right|\zeta/a^2\,\underline{e}_1 \otimes \underline{e} = -\sigma^{r}A_s\zeta/a\ \underline{e}_1 \otimes \underline{e}_1 = -N\zeta/a\ \underline{e}_1 \otimes \underline{e}_1 \end{aligned} \tag{A.12}$$

where $N = \sigma^{r}A_s$ is the axial resultant force in the reinforcement associated with the stress field $\underline{\underline{\sigma}}^{r}$.

The above defined piecewise continuous stress fields must comply with the following strength conditions:

$$\begin{cases} \underline{\underline{\sigma}}^{rc}(\underline{\xi}) = \underline{\underline{\sigma}}^{c}(\underline{\xi}) \in G_c(\xi_3) & \text{for } \underline{\xi} \in \mathcal{A} - \mathcal{A}_r \\ \underline{\underline{\sigma}}^{rc}(\underline{\xi}) = \underline{\underline{\sigma}}^{c}(\underline{\xi}) + \sigma^{r}\,\underline{e}_1 \otimes \underline{e}_1 \in G_r(\xi_3) & \text{for } \underline{\xi} \in \mathcal{A}_r \end{cases} \tag{A.13}$$

where G_r is the strength domain of the reinforcing material (steel) which may be for instance a von Mises yield strength condition with f_y as uniaxial tensile-compressive resistance.

It should be kept in mind that the *reinforcement volume fraction* of the reinforcing material, defined as $\eta = \left|\mathcal{A}_r\right|/\left|\mathcal{A}\right| = A_s a/ha^2 = A_s/ha$, is very small, typically less than 1%:

$$\eta << 1 \tag{A.14}$$

whereas at the same time the strength properties of the reinforcing material (steel) characterized by G_r are much higher than those of the plain concrete (notably its tensile strength which is taken here equal to zero):

$$f_y >> f_c (>> f_t = 0) \tag{A.15}$$

Under such particular conditions, where the concrete material can be viewed as a fiber-composite material made of a concrete matrix reinforced by *thin*, but *highly resistant*, *linear inclusions*, it may be shown by adopting the same line of reasoning as that followed by de Buhan *et al.* 2017 or de Buhan P and Taliercio, 1991 in the context of the *yield design periodic homogenization method*, that the *second* strength conditions of (A.13) may be rewritten as:

$$\left|\sigma^r\right| \le f_y \rightarrow \left|A_r \sigma^r\right| = \left|N\right| \le A_r f_y = N_0 \tag{A.16}$$

As a consequence, the following *lower bound estimate* of $\mathcal{G}_{rc}^{\hom}$ is obtained:

$$\mathcal{G}_{rc}^{\hom} \supseteq \mathcal{G}_{rc}^{\mathrm{LB}} = \left\{ \begin{array}{c} \underline{\underline{N}} = (1/a^2)\int_{\mathcal{A}} \sigma^c_{\alpha\beta}(\underline{\xi})\, \mathrm{d}\mathcal{A} + N/a\ \underline{e}_1 \otimes \underline{e}_1 \\ (\underline{\underline{N}}, \underline{\underline{M}}) \text{ s.t. } \underline{\underline{M}} = -(1/a^2)\int_{\mathcal{A}} \xi_3 \sigma^c_{\alpha\beta}(\underline{\xi})\, \mathrm{d}\mathcal{A} - \zeta N/a\ \underline{e}_1 \otimes \underline{e}_1 \\ \underline{\underline{\sigma}}^c(\underline{\xi}) \in G_c(\xi_3) \text{ and } \left|N\right| \le N_0(\zeta) \end{array} \right\} \tag{A.17}$$

or:

$$\mathcal{G}_{rc}^{\hom} \supseteq \mathcal{G}_{rc}^{\mathrm{LB}} = \mathcal{G}_c^{\hom} \oplus \mathcal{G}_r^{\hom} \tag{A.18}$$

The reciprocal inclusion $\mathcal{G}_{rc}^{\hom} \subseteq \mathcal{G}_c^{\hom} \oplus \mathcal{G}_r^{\hom}$ may be proved by using the kinematic approach, thus justifying the result (A.8).